Acta Cryst. (1982). A**38**, 780–789

High-Resolution Electron Microscopy of the Incommensurate Structure in $Sr_2Nb_2O_7$

BY N. YAMAMOTO*

Department of Physics, Tokyo Institute of Technology, Oh-Okayama, Meguro-ku, Tokyo 152, *Japan*

(*Received* 29 *October* 1981; *accepted* 14 *May* 1982)

Abstract

The incommensurate structure of strontium diniobate, $Sr_2Nb_2O_7$, is formed below 488 K with a one-dimensional lattice modulation along the [100] direction. A model of the atom displacements due to this lattice modulation has been proposed from an analysis of the systematic extinction of the extra reflections due to the incommensurate structure. High-resolution electron microscopy clearly reveals the lattice modulation in the incommensurate phase. The observed images are well interpreted by image simulation of the proposed model.

1. Introduction

Some of the $A_2B_2O_7$-type oxide compounds have a structure composed of slabs of distorted cells of perovskite-type structure rather than the pyrochlore-type structure of $Cd_2Nb_2O_7$. Recently, their physical properties were investigated by using synthesized single crystals (Nanamatsu, Kimura, Doi & Takahashi, 1971; Nanamatsu, Kimura & Kawamura, 1975). Strontium diniobate ($Sr_2Nb_2O_7$) is one of these materials which has a ferroelectric phase below 1615 K in which spontaneous polarization arises along the c axis of its orthorhombic lattice. There is another type of ferroelectric transition at 117 K. The perovskite-type slabs are stacked along the b axis, so the crystal is easily cleaved parallel to the (010) plane. The crystal structure of $Sr_2Nb_2O_7$ has been analyzed by X-ray diffraction (Ishizawa, Marumo, Kawamura & Kimura, 1975). It was reported that at room temperature the structure is orthorhombic with space group $Cmc2_1$ and lattice parameters $a = 3{\cdot}933$, $b = 26{\cdot}726$ and $c = 5{\cdot}683$ Å. Scheunemann & Müller-Bushbaum (1975), on the other hand, reported space group $Pbn2_1$ with a doubling of the a parameter. Very recently, electric and dielectric anomalies were observed at 488 K (Ohi, Kimura, Ishida & Kakinuma, 1979), which suggested the existence of a structural phase transition. An electron microscope study by the present author clearly revealed that a normal–incommensurate phase transition is responsible at this temperature (Yamamoto, Yagi, Honjo, Kimura & Kawamura, 1980).

In the present paper detailed observations and analyses of the electron diffraction pattern from the incommensurate phase are described. Then we propose a model for the atom displacements which produce the incommensurate lattice modulation. High-resolution electron microscope images reveal the modulated lattice as well as the fundamental lattice. The images were calculated by using the multi-slice method and were compared with the observed ones to test the proposed model of the atom displacements.

2. Experimental

Single crystals of $Sr_2Nb_2O_7$ were grown by a floating zone technique using an NEC infrared heating furnace (Takahashi, Nanamatsu & Kimura, 1972). The crystal was crushed into fine fragments in an agate mortar. The fragments were floated in a solution of acetone and were scooped up on copper grids coated with carbon. These specimens were examined with a JEM 200CX electron microscope equipped with a goniometer stage and a high-resolution pole piece ($C_s = 1{\cdot}2$ mm). The exposure time for recording the high-resolution images was usually 2·8 s or less at a magnification of 350 000–500 000 in order to avoid the effect of specimen drift due to mechanical and electrical instability.

3. Analysis of the electron diffraction patterns

3.1. *Exinction of the extra diffraction spots in the incommensurate phase*

Fig. 1 shows diffraction patterns from $Sr_2Nb_2O_7$ at room temperature. The electron beam is parallel to the

* Present address: Department of Physics, Arizona State University, Tempe, Arizona 85287, USA.

0567-7394/82/060780-10$01.00

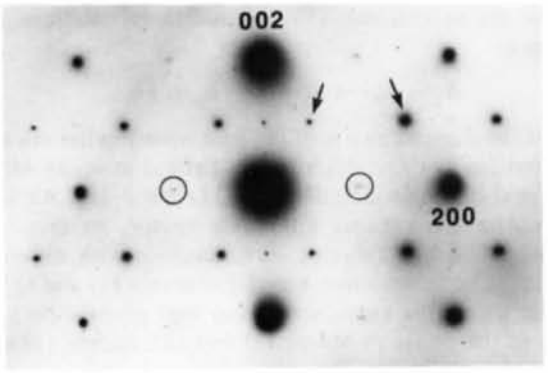

(*a*)

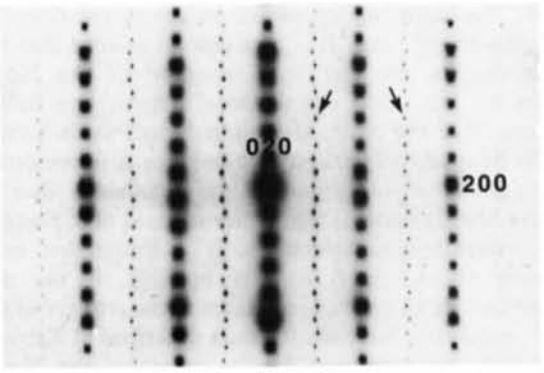

(*b*)

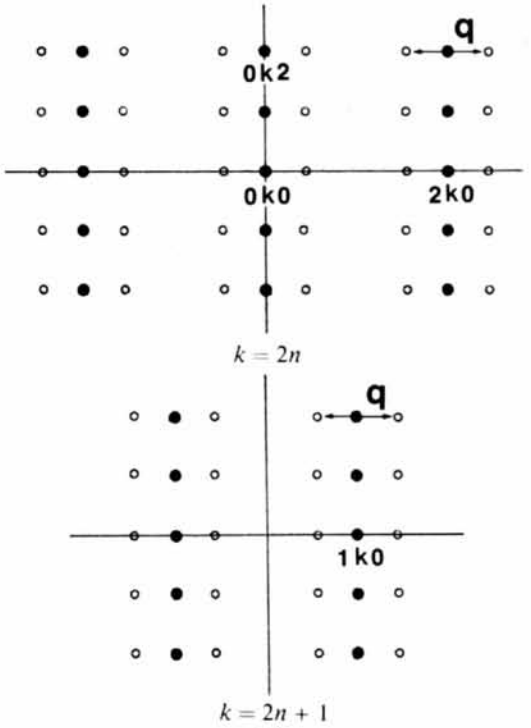

(*c*)

Fig. 1. Diffraction patterns from $Sr_2Nb_2O_7$ (*a*) in the [010] and (*b*) in the [001] orientation at room temperature. Arrows indicate extra diffraction spots appearing below 488 K. (*c*) The arrangement of the diffraction spots in reciprocal space.

[010] axis of the high-temperature normal phase† in (*a*) and to the [001] axis in (*b*). In the incommensurate phase below 488 K weak extra diffraction spots appear at irrational positions as indicated by arrows in Fig. 1(*a*) and (*b*). Their positions are very close to $h + \frac{1}{2}, k, l$, but are displaced slightly along the $[100]^*$ direction as shown in Fig. 1(*b*). The fundamental spots have systematic absences of hkl, $h + k$ odd and $h0l$, l odd. The wave vector for the lattice modulation wave in the incommensurate phase can be chosen as $\mathbf{q} = q\mathbf{a}^* = \pm(\frac{1}{2} - \delta)\mathbf{a}^*$, where δ indicates deviation of the spots from the half-integer position. Then the extra spots appear at the following positions:

$$h \pm q, k, l \quad : h + k = 2n, k \neq 0 \qquad (1a)$$

$$h \pm q, 0, l \quad : h = 2n, l = 2n + 1. \qquad (1b)$$

There are also seen very weak diffraction spots enclosed by circles in Fig. 1(*a*). They arise from multiple scattering, since they do not appear in the [001] orientation (Fig. 1*b*). The fact that they are split clearly shows that the extra diffraction spots are at irrational positions. It is noticed that there are no second-order extra diffraction spots. If they really existed, they should appear, for example, around the 101 position in Fig. 1(*a*), or the 120 position in (*b*). The value of δ at room temperature is 0·010 and decreases with decreasing temperature, but has a finite value even at 55 K (Yamamoto, Yagi, Honjo, Kimura & Kawamura, 1980). It is not yet clear whether an incommensurate–commensurate phase transition occurs at this low temperature or not.

3.2. *A model of atom displacements in the incommensurate phase*

A model of the atom displacements can be derived from the systematic extinction of the extra diffraction spots mentioned in § 3.1. The displacement of the kth atom in the nth unit cell aligned along the a axis can be expressed as

$$\begin{aligned} \Delta\mathbf{r}_{nk} &= \mathbf{A}_k \sin(2\pi\mathbf{q}.\mathbf{r}_{nk} + \varphi_k) \\ &= \mathbf{A}_k \sin[2\pi(nq + \mathbf{q}.\mathbf{r}_k) + \varphi_k], \end{aligned} \qquad (2)$$

where $\mathbf{r}_{nk}$ is the ideal position vector of the atom in the crystal, $\mathbf{r}_k$ that in the unit cell, $\mathbf{q}$ the modulation wave vector, and $\mathbf{A}_k$ and φ_k the amplitude vector and phase of the modulation wave, respectively. Higher harmonic terms are neglected, since the higher-order extra diffraction spots are not observed. The scattering amplitude from the crystal is given as

$$F(\mathbf{s}) = \sum_n \sum_k f_k \exp[2\pi i\mathbf{s}.(\mathbf{r}_{nk} + \Delta\mathbf{r}_{nk})], \qquad (3)$$

† In the normal phase above 488 K the crystal is considered to have the structure reported by Ishizawa *et al.* (1975) so the crystallographic directions and the indices of the reflections in the incommensurate phase will always be referred to the orthorhombic crystal axes of the normal phase throughout this paper.

where f_k is an atom form factor of the kth atom, and $\mathbf{s}$ is a scattering vector. By using the relationship

$$\exp(iZ\sin\theta) = \sum_{m=-\infty}^{\infty} J_m(Z)\exp(im\theta),$$

we have

$$F(\mathbf{s}) = \sum_k f_k \exp[2\pi i\mathbf{s}.\mathbf{r}_k] \times \sum_{m=-\infty}^{\infty} J_m(2\pi\mathbf{s}.\mathbf{A}_k)\exp[im(2\pi\mathbf{q}.\mathbf{r}_k + \varphi_k)] \times \sum_n \exp[2\pi i(\mathbf{s} + m\mathbf{q}).\mathbf{R}_n], \quad (4)$$

where J_m is the Bessel function of mth order, and $\mathbf{R}_n$ is the position vector of the origin of the nth unit cell. To a first approximation $J_0 \simeq 1$ and $J_{\pm1}(2\pi\mathbf{s}.\mathbf{A}_k) \simeq \pm\pi\mathbf{s}.\mathbf{A}_k$ for the condition $\mathbf{s}.\mathbf{A}_k \ll 1$, and the higher-order terms J_m ($|m| > 2$) can be neglected. The term of J_0 gives the scattering amplitude of the fundamental diffraction spot and the terms of $J_{\pm1}$ give that of the first-order satellite diffraction spots, which is proportional to the following term,

$$\Delta F(\mathbf{s}) \propto \pm\sum_k f_k(\mathbf{s}.\mathbf{A}_k)\exp[2\pi i\mathbf{s}.\mathbf{r}_k] \times \exp[\pm(2\pi i\mathbf{q}.\mathbf{r}_k + i\varphi_k)]\, G(s_x \pm q)\, G(s_y)\, G(s_z), \quad (5)$$

where s_x, s_y, s_z are components of $\mathbf{s}$, and $G(s)$ is $\sin(\pi Ns)/\sin(\pi s)$, where N is the number of unit cells in the crystal. $G(s_x \pm q)$ has a finite value only when $s_x \pm q = h$(integer), so $\Delta F(\mathbf{s})$ has peaks at the positions $\mathbf{s} = [h \pm q, k, l]$.

The extinctions of the extra diffraction spots are very similar to those of the fundamental spots except for the extra spots around the $h0l$ spots. In the normal phase with the space group $Cmc2_1$, all atoms are positioned at the 4(a) sites described in Table 1. It is proposed that the 4(a) site atoms are displaced with a correlation between each other in the incommensurate phase. For such atom displacements $\Delta F(\mathbf{s})$ must satisfy the extinction rules of the extra diffraction spots at positions of $|h \pm q, k, l|$ with any h,k,l. We substitute the coordinates of the 4(a) sites in (5) and find the relationships between the amplitude vectors and phases of the four atoms which make $\Delta F(\mathbf{s})$ equal to zero in accordance with the extinction rules. The first rule of (1a) gives the following relationships:

$$\mathbf{A}_1 = \mathbf{A}_2, \quad \mathbf{A}_3 = \mathbf{A}_4, \quad \varphi_1 = \varphi_2, \quad \varphi_3 = \varphi_4. \quad (6)$$

Table 1. *Displacements of atoms* (1) *to* (4)

$\mathbf{r}_k$	$\mathbf{r}_{nk}$
(1) 0,y,z	$\mathbf{A}_k \sin[2\pi n/M + \varphi_k]$
(2) $\frac{1}{2}$, $\frac{1}{2}+y$, z	$\mathbf{A}_k \sin[2\pi(n/M + 1/2M) + \varphi_k]$
(3) 0, $\bar{y}$, $\frac{1}{2}+z$	$\mathbf{A}_k \sin[2\pi(n/M + \frac{1}{2}) + \varphi_k]$
(4) $\frac{1}{2}$, $\frac{1}{2}+\bar{y}$, $\frac{1}{2}+z$	$\mathbf{A}_k \sin[2\pi(n/M + 1/2M + \frac{1}{2}) + \varphi_k]$

From the second rule (1b) the additional relations are given as

$$\mathbf{A}_1 = \mathbf{A}_3 \quad \text{and} \quad \varphi_1 - \varphi_3 = \pm\pi. \quad (7)$$

Then the displacements of the four atoms in the nth cell are written as those described in Table 1 in which Ma is a period of the modulation wave, *i.e.* $M = 1/q$. All four atoms have the same amplitude vector, so they are displaced along the same direction, but with different phases. The modulation waves for atoms (1) and (2) in Table 1 have the same phase, and their phase differs by π from the phase of atoms (3) and (4). Atoms (1) and (3) are in the same perovskite slab and atoms (2) and (4) are in the neighbouring slab.

The displacements of all the atoms in the unit cell obey the above rules. It is plausible to assume that the displacements are due to a *rotation* of the NbO_6 octahedra around a certain axis without any deformation, since the phase transition concerned is known *not* to be a ferroelectric transition. For a ferroelectric transition, a *deformation* of the octahedra due to relative shifts of anions and cations would take place in the perovskite-type structures. It is found that only rotation about the b axis is possible, if the displacements of all the oxygen atoms at the corners of the NbO_6 octahedra have the formula described in Table 1. This may be supported by the result of the X-ray analysis of $Ca_2Nb_2O_7$ (Ishizawa, Marumo & Iwai, 1980), which has the same type of structure as $Sr_2Nb_2O_7$ and undertakes successive phase transitions similar to those of $Sr_2Nb_2O_7$, in which the space group of the crystals changes as $Cmcm \rightarrow Cmc2_1 \rightarrow P2_1$ with decreasing temperature. It was reported that the rotational displacements of the oxyen octahedra around the b axis occur in the material at the phase transition from $Cmc2_1$ to $P2_1$. The displacements of the oxygen atoms corresponding to the rotation of the octahedra proposed here are shown in Fig. 2. In Fig. 2(c) arrows inside the octahedra indicate the directions of the rotation. The Sr atoms are considered to displace nearly in the c direction accompanied by the displacements of the oxygen atoms. For simplicity the atom displacements are depicted in Fig. 2 as if the modulation wave had a period of $2a$ and a phase of $\varphi = \pi/4$, so that the atom displacements in the neighbouring slabs have the same magnitude. The model mentioned here will be tested in a later section.

3.3. *Lattice modulation in the incommensurate phase*

Generally, lattice modulations in incommensurate phases can be divided into two types in terms of the structural aspect, *i.e.* spatially continuous or spatially discontinuous, both of which can give rise to similar extra diffraction spots at irrational positions. The former is a displacive-type modulation which has been reported for many materials such as the transition-

metal dichalogenides (Van Landuyt, Van Tendeloo & Amelinckx, 1974*a*,*b*, 1976; Wilson, di Salvo & Mahajan, 1975) and ferroelectric crystals (Hoshino & Motegi, 1967; Shiozaki, 1971; Iizumi, Axe, Shirane & Shimaoka, 1977). The latter has been reported for many alloys (Sato & Toth, 1961), oxides (Iijima & Cowley, 1974; Bando & Iijima, 1980) and sulphides (Nakazawa, Yamamoto & Morimoto, 1979), which is usually accompanied by periodic or nonperiodic arrays of crystal defects such as out-of-phase boundaries. The sharp splits of superlattice reflections from ordered alloys containing antiphase domains were studied theoretically by Fujiwara (1957).

Here we consider two simple one-dimensional models for the lattice modulation of $Sr_2Nb_2O_7$, a sinusoidal modulation and a periodic array of antiphase boundaries. They are schematically shown in Figs. 3(*a*) and (*b*), respectively. In Fig. 3(*a*), the sinusoidal modulation with a period slightly larger than $2a$ gives displacements of atoms as indicated by arrows. It is a longitudinal wave, so the arrows show magnitudes of the atom displacements but not directions of them. The form factor of the nth atom for the **h** reflection is written as

$$F_n(\mathbf{h}) = f\exp|2\pi i(\mathbf{h}.\mathbf{A})\sin(2\pi n/M)|, \qquad (8)$$

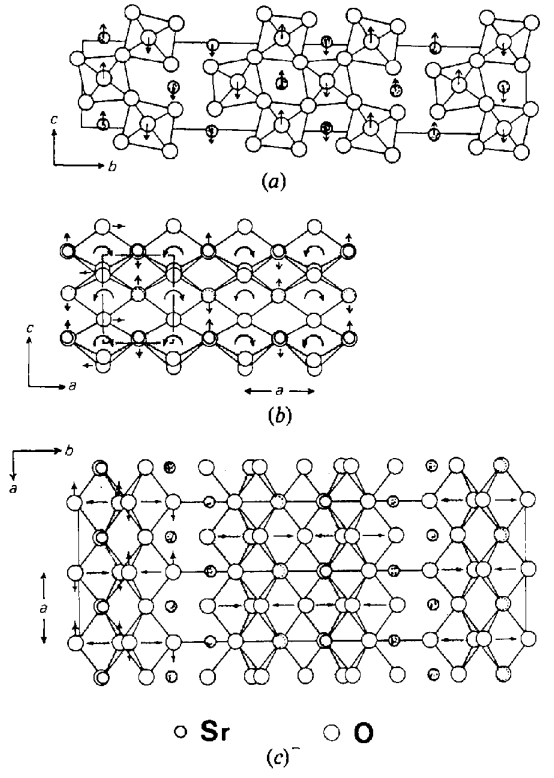

Fig. 2. The model of the atom displacements in the incommensurate phase: (*a*), (*b*) and (*c*) show the structure viewed along the *a*, *b*, and *c* axes. Nb atoms are located inside the oxygen octahedra.

where **A** and M have the same meaning as before, and f is an atom form factor and is kept constant for simplicity. Then the value of δ is given as

$$\delta = \tfrac{1}{2} - 1/M = 1/2N, \qquad (9)$$

where N is the number of unit cells through which the modulation wave changes its phase by π (see Fig. 3). For an array of antiphase boundaries in the lattice where atoms displace in opposite directions alternately, a form factor of the atom is written as

$$F_n(h) = f\exp|\pm 2\pi i\mathbf{h}.\mathbf{A}|. \qquad (10)$$

The two models give the intensity distributions in the diffraction pattern similar to each other as shown in Figs. 4(*a*) and (*b*), respectively. In (*a*) the diffraction peak near the positions of $h = 1/2$ and $3/2$ are satellite reflections around the nearest fundamental spots, while in (*b*) those peaks are considered to be split spots of the ordered structure $\delta = 0$ (Sato & Toth, 1961).

It seems to be difficult to distinguish between the two types of modulations from the analysis of the diffrac-

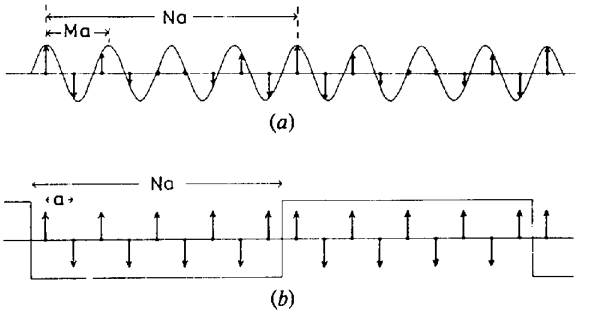

Fig. 3. One-dimensional models of the incommensurate lattice modulation: (*a*) a sinusoidal modulation and (*b*) an array of antiphase boundaries. Arrows indicate magnitudes of atom displacements.

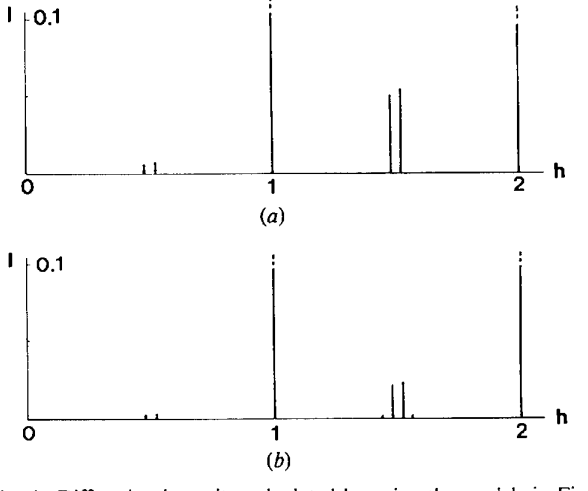

Fig. 4 Diffraction intensity calculated by using the models in Fig. 3(*a*) and (*b*). In both cases, $N = 25$ ($\delta = 0{\cdot}02$) and $\mathbf{A} = 0{\cdot}05\mathbf{a}$.

tion pattern. However, in case of $Sr_2Nb_2O_7$ the extra diffraction spots show an extinction in which only one of the two peaks near the half-integer positions disappears. It is found from the above argument that a spatially discontinuous modulation cannot explain this type of extinction, since it always produces a pair of spots at both sides of the half integer positions. Therefore only a spatially continuous modulation can be considered as a lattice modulation of $Sr_2Nb_2O_7$. If the higher-order harmonic terms in the modulation wave were considerably large, they should give rise to higher-order satellite diffraction spots and reduce the extinction. These effects are not found in the diffraction pattern in Fig. 1. Thus the lattice modulation is expected to be very close to the simple sinusoidal modulation.

4. High-resolution electron microscopic study of the incommensurate lattice modulation

4.1. *Imaging of the lattice modulation*

High-resolution electron micrographs of the crystals were taken in the |010|, |001|, |011| and |201| orientations. For the crystals of the |010|, |001|, and |201| orientations, weak lattice-fringe images showing the modulated lattices were observed at certain crystal thicknesses and defocuses. But the relationship between the fundamental lattice and the modulated lattice was not clearly seen in those images. On the other hand, the crystal in the |011| orientation gave a clear image of both of them as shown in Fig. 5(*a*), which is an electron micrograph taken under the diffraction condition shown in (*b*). The circle in (*b*) shows the size of the objective aperture. The thickness of the crystal increases from lower to upper parts of the micrograph. Several steps on the cleaved surface with a height of one slab thickness (1·3 nm) are contrasted at positions indicated by triangles. Broad lattice fringes indicated by the arrows *P* and *Q* are also seen which are produced by the diffraction spots near the positions $\frac{1}{2}00$ and $\frac{1}{2}\bar{1}1$, respectively, and due to the modulated lattice of the incommensurate structure. The reflection near the $\frac{1}{2}00$ position is a forbidden reflection, but appears in the diffraction pattern from this orientation due to the multiple-scattering effects. It is noted that the contrast of the modulated lattice fringes increases with crystal thickness and it is hardly seen in the thin regions. These fringes were stable during the observation and appeared homogeneously within the region of at least a few hundred nm across.

Fig. 5(*c*) shows a magnified image of the region enclosed by the rectangle in (*a*). Fine black and white spots are seen which are produced by the fundamental reflections giving the image of the fundamental lattices. The spacing between the white spots along the *a* axis corresponds to the lattice parameter *a*. The upper vertical short lines in the middle of (*c*) show the positions of the white spots, with an interval of 2*a*. The lower vertical lines show the white positions of the fringes (marked *P* in Fig. 5*a*) due to the modulated structure. The spacing of the latter fringes is slightly larger than 2*a*, and the upper and lower vertical lines gradually shift with each other from left to right in the figure. This clearly shows the spatially continuous nature of the lattice modulation in the incommensurate phase. The relative shift of the 16th lines amounts to *a*, which corresponds to a value of δ of 0·015.

Figs. 6(*a*) to (*d*) show the images of a through-focus series taken from another region but in the same orientation and with nearly the same crystal thickness as that of Fig. 5(*c*). The image in (*d*) is very similar to that of Fig. 5(*c*). The contrast of the modulated lattice fringes changes with defocusing; the fringes are seen in (*a*) and (*d*), but not in (*b*) and (*c*).

4.2. *Image simulation*

First, for simplicity we simulate the images from the fundamental structure on the basis of the multislice

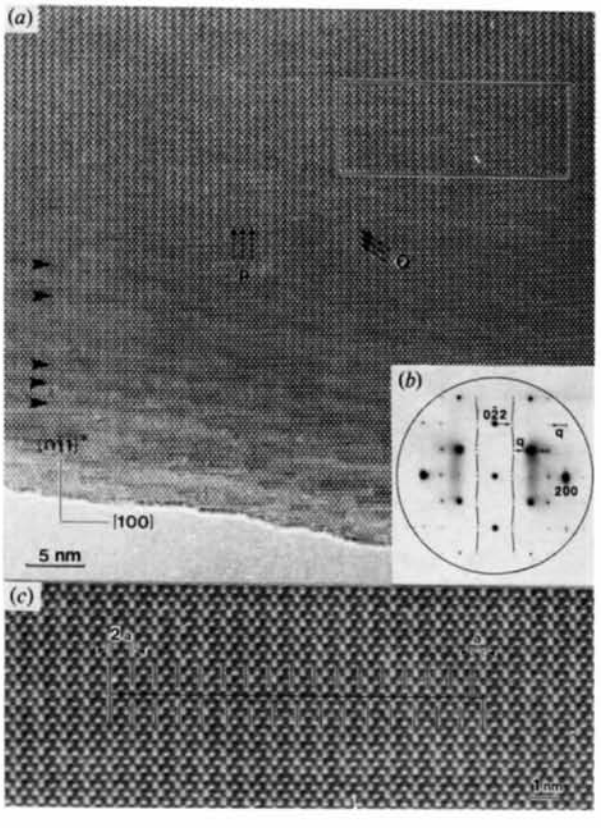

Fig. 5. (*a*) High-resolution image of the crystal in the |011| orientation, taken under the diffraction condition shown in (*b*). The fringes marked *P* and *Q* show the modulated lattices in the incommensurate phase. (*c*) The magnified image inside the rectangle in (*a*), clearly revealing the spatially continuous lattice modulation (see text).

method (Goodman & Moodie, 1974; Cowley, 1975), in order to find the crystal thickness and the value of defocus for the observed images. The atom coordinates reported by Ishizawa *et al.* (1975) were used as those of the fundamental structure. The direction of the incident electron beam is along the |011| axis, so slices are perpendicular to the |011| axis with a thickness Δz of $(b^2 + c^2)^{1/2}$ corresponding to one unit-cell dimension, *i.e.* $\Delta z = 2{\cdot}74$ nm (see Fig. 7). The projected potential along the |011| direction has cell dimensions, a and $d_{0\bar{1}1}$ in the orthogonal directions on the plane of the slice, where $d_{0\bar{1}1}$ is the spacing of the $(0\bar{1}1)$ planes (0·56 nm). The number of beams used is 1024 (32 × 32). Fig. 8(i)(*a*) shows the calculated projected potential. The projected cell is shown by the rectangle. The potential peaks concentrate on the mirror planes at the positions of $x = 0$ and $x = \frac{1}{2}$, since every atom is located on the mirror planes (see Fig. 2). The conventional values of the instrumental parameters of the JEM 200CX electron microscope were used for the image calculation; the coefficient of spherical aberration of the objective lens $C_s = 1{\cdot}4$ mm, the coefficient of chromatic aberration of the objective lens $C_c = 1{\cdot}4$ mm and the instability of the high voltage and the objective lens current $\Delta V/V = 2\Delta I/I = 2 \times 10^{-6}$. The semi-angle of the beam divergence is 0·45 mrad corresponding to a condenser aperture of diameter 100 μm, and the objective aperture includes all reflections less than 0·75 $Å^{-1}$ in reciprocal space. The effects of chromatic aberration and beam divergence were treated by using envelope functions (Fejes, 1977). Simulations were done for many crystal thicknesses and defocus values, and the simulated images were compared with observed images. It was found that calculated images similar to those observed are found for the crystal thickness of $8\Delta z$ (21·89 nm). These images for several defocus values are shown in Figs. 8(i)(*b*) to (i)(*h*), and the images of (i)(*b*), (i)(*d*), (i)(*e*) and (i)(*f*) fit well with the observed images in Figs. 6(*a*) to (*d*) respectively, except for the modulated lattice-fringe contrast.

Next we consider the contribution to the image contrast from the atom displacements due to the modulation wave. We use the model shown in Fig. 2 and assume, for convenience, that the modulation wave has a period of $2a$ ($M = 2$). At first only the displacements of the heavy Sr atoms either in the c direction or in the a direction were considered for the calculation. The displacement with the amplitude vector of 0·02**c** gave no appreciable change in any simulated images of the through-focus series, but those with 0·03**c** and 0·04**c** gave images similar to the observed ones. However, images given for the amplitude vector of 0·05**c** showed unacceptable contrast changes. The images were also calculated for the same conditions except that the phase of the modulation wave was taken as zero or $\pi/2$ instead of $\pi/4$. These images had stronger contrast due to the modulation wave than those for the phase of $\pi/4$, but in this case the calculated intensities of forbidden reflection such as the 011 and 100 reflections became comparable with

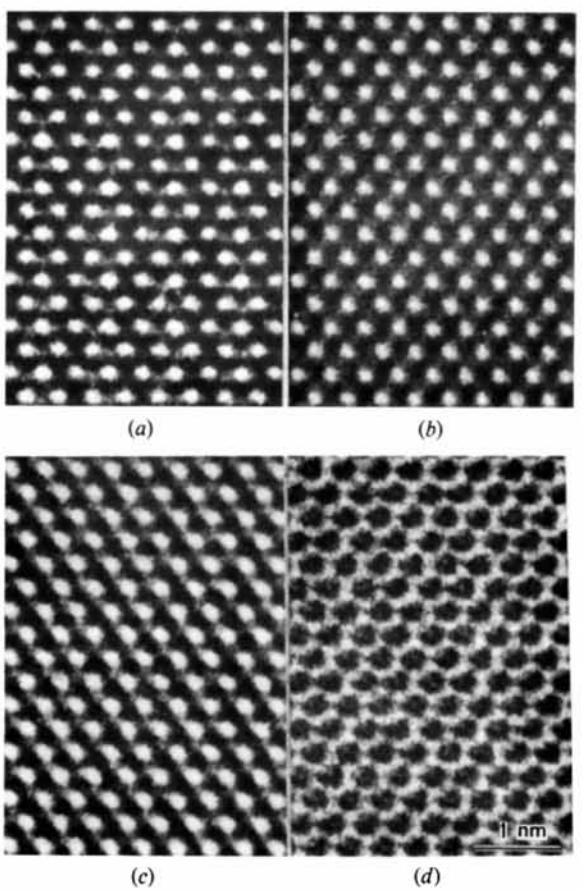

Fig. 6. The through-focus images from the |011| crystal with a thickness nearly the same as that in Fig. 5(*c*).

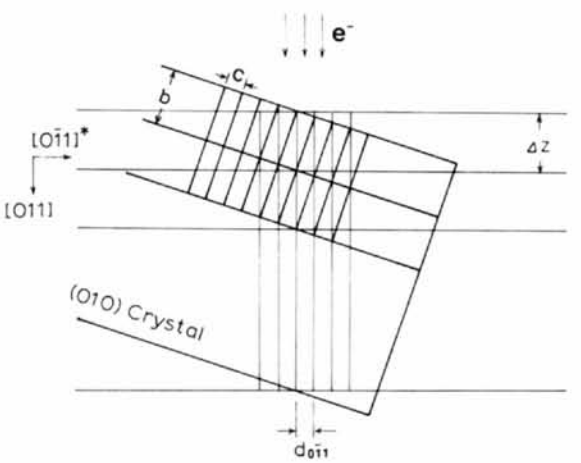

Fig. 7. The arrangement of the crystal and the electron beam under which the images in Figs. 5 and 6 were taken. Δz is a slice thickness for the image simulation by the multi-slice method.

the extra reflections though they are both extremely small for the phase of $\pi/4$. Thus it is expected that the c component of the amplitude vector for the Sr atoms is in the range between 0·02**c** and 0·05**c**, *i.e.* 8 to 20 Pm. With the displacement of Sr atoms in the a direction the calculated images for the amplitude vector of 0·04**a** showed no contrast change, but those for the amplitude vector of 0·06**a** gave images different from the observed ones. Although the images are not sensitive enough to estimate the a component of the amplitude vector, it can be safely said that the a component is less than 0·04**a**, since even for this value the calculated intensity of the forbidden 100 reflection became comparable to those of the extra reflections.

Figs. 8(ii)(*a*) to (ii)(*h*) show the case of good fit with the observed images; (*a*) is the projected potential, and figures from (*b*) to (*h*) are the images of the through-focus series calculated for an amplitude vector of the modulation wave of 0·03**c** for the Sr atoms, and 0·04**a** and 0·03**c** for the oxygen atoms. Those displacements of oxygen atoms (11 Pm) correspond to a rotation of the NbO_6 octahedra by 3·3° around the b axis. The phases of the modulation wave φ_k were taken as $\pi/4$ for each atom. The contribution of the displacements of the oxygen atoms to the images is small in comparison with that of the Sr atoms, but it was found that they enhance the contrast of the modulation fringes to some extent. Figs. 8(ii)(*b*), (*d*), (*e*), (*f*) fit well with the observed images of Figs. 6(*a*) to (*d*), respectively. The modulation of the contrast with a period of $2a$ appears in (ii)(*b*) and (ii)(*f*), but not in (ii)(*d*) and (ii)(*e*). (Notice the faint image contrast among the strong white spots.)

4.3. *Interpretation of the images*

Figs. 9(*a*) and (*b*) show the variation of the intensities and phases of several reflections with crystal thickness (t), which are the results of the multi-slice calculation for the images of Fig. 8(ii). The intensities of the $\frac{1}{2}00$ and $\frac{1}{2}\bar{1}1$ reflections are seen to increase monotonically with thickness and become strong enough to contribute to the image profiles at a thickness of $8\Delta z$. This agrees with the contrast variation of the modulated lattice fringes mentioned in Fig. 5(*a*). However, at a thickness of $8\Delta z$ the intensities and phases of the fundamental reflections are different from those expected by the kinematical approximation, so the image does not reproduce the structure.

Here we consider the effect of defocusing on the images. The wave function of the electron at the bottom of the crystal is described as

$$\psi(\mathbf{r}) = \sum_{\mathbf{h}} \Psi_{\mathbf{h}} \exp(2\pi i \mathbf{h}.\mathbf{r}), \tag{11}$$

where $\Psi_{\mathbf{h}}$ is the amplitude of the **h** reflected beam. The intensity on the image plane is given as

$$I(\mathbf{r}) = \left| \sum_{\mathbf{h}} \Psi_{\mathbf{h}} \exp(2\pi i \mathbf{h}.\mathbf{r}) \exp[i\chi(\mathbf{h})] \right|^2, \tag{12}$$

where $\chi(\mathbf{h})$ is a phase factor given in terms of the defocus Δf, the wavelength of the electron beam λ, and the spherical aberration coefficient, C_s, as $\chi(\mathbf{h}) = \pi\Delta f\lambda\mathbf{h}^2 + (\pi/2)C_s\lambda^3\mathbf{h}^4$.

Large terms coupled with the transmitted beam in (12) are given for axial illumination by

$$I(\mathbf{r}) = \sum_{\mathbf{h}} 2|\Psi_{\mathbf{h}}\Psi_0|\cos[2\pi(\mathbf{h}.\mathbf{r}) + \chi(\mathbf{h}) + \theta_{\mathbf{h}} - \theta_0| + \ldots, \tag{13}$$

where $\theta_{\mathbf{h}}$ is the phase of $\Psi_{\mathbf{h}}$. This expression indicates that the image is composed of many lattice fringes. The lattice fringes for the **h** reflection depend on the phase factor $\chi(\mathbf{h})$ or the value of defocus, Δf, so defocusing causes a shift of the lattice fringes due to the change of

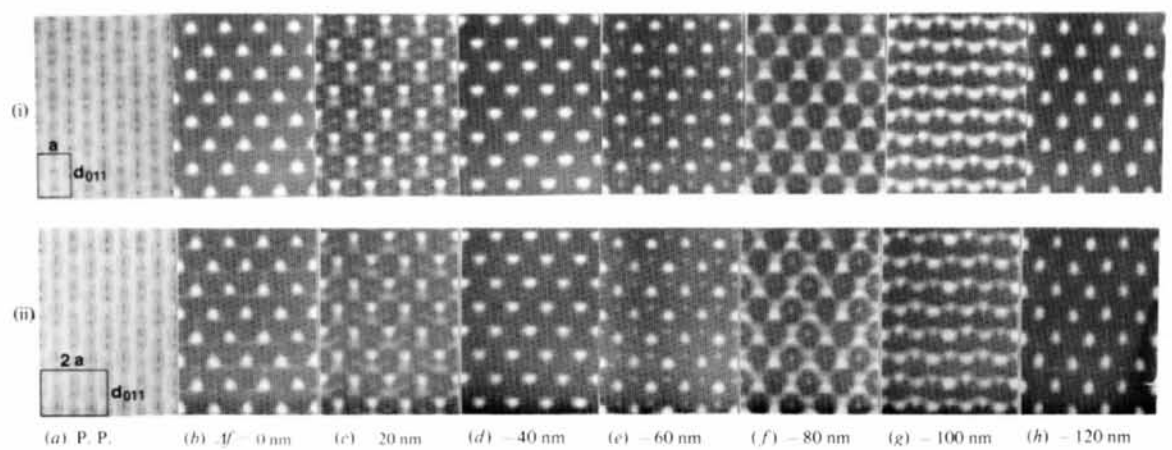

Fig. 8. Simulated images (i) for the normal structure and (ii) for the modulated structure ($M = 2$). The crystal thickness is $8\Delta z$. The images in column (*a*) show projected potentials (P.P.) along the [011] axis and those in columns (*b*) to (*h*) are images of the through-focus series.

this phase factor. If the change of $\chi(\mathbf{h})$ by defocusing amounts to 2π, the lattice fringes shift to the same position as before. This arises with the defocus period of $\Delta f_f = 2/\lambda|\mathbf{h}|^2$ for the $\mathbf{h}$ reflection (Fourier images; Cowley, 1975). In the case of centrosymmetric crystals, $\Psi_{\mathbf{h}} = \Psi_{-\mathbf{h}}$, so the lattice fringes produced by the $\mathbf{h}$ and $-\mathbf{h}$ reflections do not move but change their contrast as the defocus varies. However, if $\Psi_{\mathbf{h}} \neq \Psi_{\mathbf{h}}$,

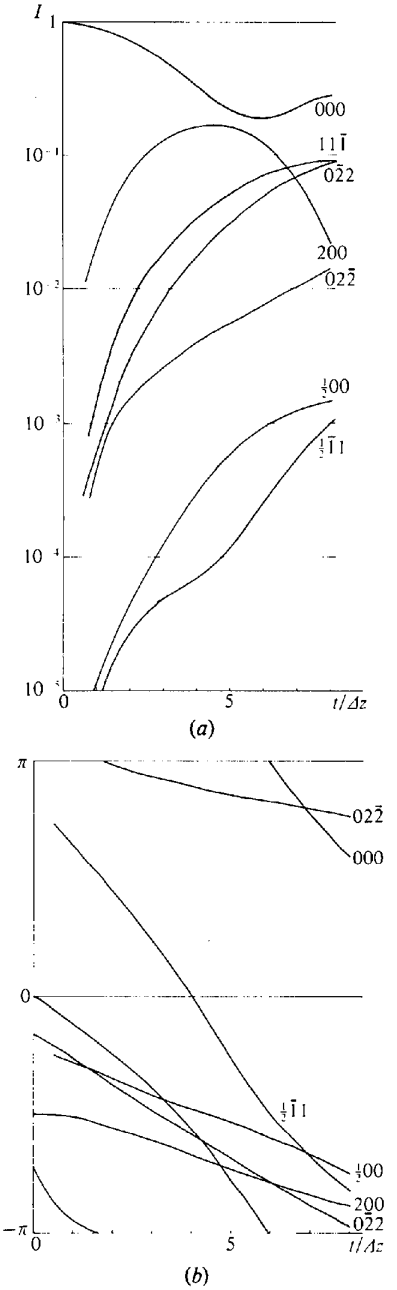

Fig. 9. Variation of (*a*) intensities and (*b*) phases of several reflections with crystal thickness calculated by the multislice method.

the dominant lattice fringes will be seen to move by defocusing.

In our case the images are mainly produced by the lattice fringes of the (02$\bar{2}$), (1$\bar{1}$1) and (200) planes. The crystal is noncentrosymmetric and it was found in the calculation that $|\Psi(0\bar{2}2)|$ is larger than $|\Psi(02\bar{2})|$ by a factor of 2·4 at the crystal thickness of $8\Delta z$, and $|\Psi(1\bar{1}1)| > |\Psi(11\bar{1})|$, $\Psi(200) \simeq \Psi(\bar{2}00)$. The value of Δf_f is equal to 61·6 nm for the 0$\bar{2}$2 reflection and 82·2 nm for the 1$\bar{1}$1 reflection. It is seen in Fig. 8(ii) that the lattice fringes of the 0$\bar{2}$2 reflection, which consists of arrays of the strong white spots aligned parallel to the horizontal line shift from (*b*) to (*c*) and (*d*), in both (*e*) and (*h*) locate at nearly the same position as in (*b*). In the same way the lattice fringes of the 1$\bar{1}$1 reflection which are oblique lines shift from (*b*) to (*d*) by half of the fringe spacing and come back to the initial position in (*f*). The weak modulated lattice fringes are invisible when these strong fringes enhance each other to produce a strong contrast as seen in (*d*), (*e*), and (*h*). On the other hand, they can be seen as in (*b*), (*c*), (*f*), and (*g*).

For the modulated lattice fringes due to the extra reflection near the $\frac{1}{2}00$ position, the value of Δf_f is large (493·6 nm), because of the low-order reflection. So the modulated lattice fringes shift very little by the defocus change compared with the lattice fringes of the fundamental reflections. It is noticeable that the strong white spots produced by the fundamental reflections always appear nearly on the mirror planes of the fundamental lattice in the images of the through-focus series in Fig. 8(ii). These facts give the possibility of determining precisely the phase of the modulation wave at each atom position or the spatial distribution of the atom displacements in the crystal.

Fig. 10 schematically depicts the atom displacements in the successive perovskite-type slabs due to the modulation wave, in accordance with the model mentioned in § 3.2. The figure shows a cross section of

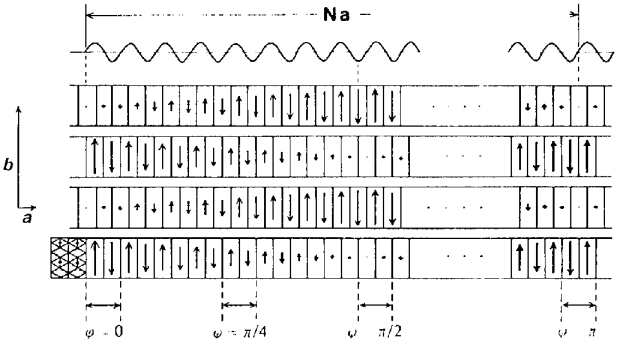

Fig. 10. Schematic representation of atom displacements in the successive perovskite slabs due to the incommensurate lattice modulation. This is a projection along the *c* axis, corresponding to Fig. 2(*c*). The modulation wave is depicted at the upper part of the figure.

the structure perpendicular to the c axis, corresponding to Fig. 2(c). The arrows indicate magnitudes of the atom displacements such as the rotation of the NbO_6 octahedra. The phase, φ, of the modulation wave at the origin of each unit cell is indicated in the lower part of the figure.

The regions with phases φ and $\varphi + \pi$ will show the same images except that they shift from each other by the lattice parameter a. We simulated the observed images shown in Fig. 5(c) by using the same parameters as those used to calculate the image of Fig. 8(ii)(f), for the different phases of $\varphi = 0$, $\pi/4$ and $\pi/2$. Fig. 11(a) is a magnified image of Fig. 5(c), and Fig. 11(b) shows the calculated images. When we notice the contrasts of the white spots aligned in the horizontal line at the level indicated by arrows 1 and 2 in Fig. 11(a), we find that along the line 1 the white spots change their contrasts alternately in the left of the micrograph but not in the right, while along the line 2 the contrast change arises in the right but not in the left. In the middle region of the micrograph the contrast of the white spots changes alternately along both of the lines. This feature repeats in the upper and lower successive lines. The calculated images for the phases of 0, $\pi/4$, and $\pi/2$ fit with the observed ones if arranged as shown in Fig. 11. Therefore, we can find the phase of the modulation wave at any position from the micrograph.

The above mentioned contrast is interpreted as the modulated lattice fringes, *i.e.* the vertical fringes P in Fig. 5. As indicated by marks B (bright) and D (dark) in Fig. 11(b), the bright fringes which locate at the positions of the white spots on the line 1 in the region of $\varphi = 0$ shift gradually with an increase of the phase. They shift by $a/2$ into the positions of the neighbouring white spots on line 2 in the region of $\varphi = \pi/2$. These features are just those described for the image of Fig. 5(c).

5. Summary and discussion

High-resolution electron microscopy is a useful method for analysing incommensurate lattice modulations of the displacive type. The intensities of the extra reflections are too weak in the thin region of the crystal to contribute to the image profile. It is necessary to treat the images in the thicker region in order to obtain information on the lattice modulation, although such images do not reveal the crystal structure even under the optimum defocus condition. From the precise comparison of the observed through-focus images with the simulated images it is found that a model of the atom displacements proposed on the basis of the analysis of the systematic extinctions of the extra reflections explains well the observed images. However, the images are not very sensitive to the atom displacements, especially for those of the oxygen atoms. The image simulation also enables us to determine the phase of the modulation wave at a particular position in the crystal.

In the calculation by the multi-slice method the slice thickness taken here seems to be too large, since the electron wave laterally spreads out by about 0·08 nm due to Fresnel diffraction when it propagates through one slice. But if we choose a thinner slice to divide the unit cell in the usual way, this makes the multislice calculation more difficult, because the lateral period of the projected potential for each slice becomes too large. In order to avoid this difficulty, the crystal was cut into

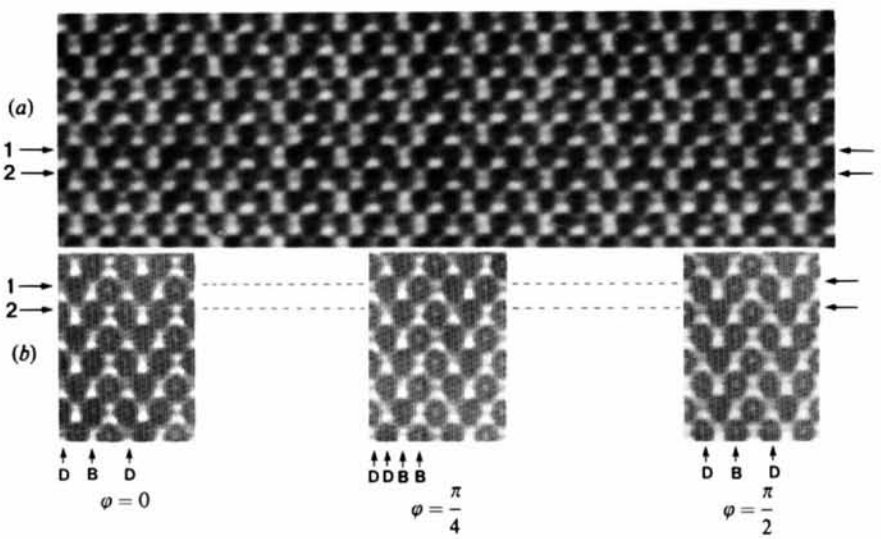

Fig. 11. (a) The magnified image of Fig. 5(c), and (b) simulated images under the same condition as that in Fig. 8(ii)(f), but for different phases. Notice the contrasts of the white spots along the lines 1 and 2.

thin slices parallel to the (010) plane to conserve the periodicity of the unit cell, and the images were calculated by the usual multislice method, using the algorithm recently proposed by Ishizuka (1982). The results of such a calculation in which the unit cell was cut into four pieces showed that the variation of the amplitudes Ψ_h of the low-order reflections with the crystal thickness is almost the same as that in Fig. 9. So we can safely say that the value of Δz used here is not large enough to affect the image calculation seriously. This is because the main profiles of the images are produced by a few of the low-order reflections.

The physical origin of the appearance of the incommensurate phase in $Sr_2Nb_2O_7$ has not yet been explained. $BaMnF_4$ also has an incommensurate phase below 247 K (Cox, Shapiro & Cowley, 1979), the structure of which is similar to $Sr_2Nb_2O_7$ except that the thickness of the perovskite-type slab is half of that in $Sr_2Nb_2O_7$. However, the lattice modulation and its properties are different from those in $Sr_2Nb_2O_7$. Recent study of the solid solutions $Sr_2(Ta_{1-x}Nb_x)_2O_7$ (Yamamoto, Nakamura, Yagi & Ohi, 1980) showed a close correlation between the incommensurate structure of $Sr_2Nb_2O_7$ and the superlattice structure of $Sr_2Ta_2O_7$. This point must be taken into account when we consider the origin of the incommensurate phase.

The author is indebted to Professors G. Honjo, and K. Yagi for their useful discussions and continuous encouragement. Thanks are also due to Dr K. Ishizuka for the fruitful discussion on the image simulation. This work was partly supported by ARO grant number DAAG-29-80-C-0080 and the NSF HREM facility at ASU.

References

BANDO, Y. & IIJIMA, S. (1980). *Proceedings of the 38th Annual Meeting of the Electron Microscopy Society of America*, pp. 166–167. Baton Rouge: Claitor.

COWLEY, J. M. (1975). *Diffraction Physics*. Amsterdam: North-Holland.

COX, D. E., SHAPIRO, S. M. & COWLEY, R. A. (1979). *Phys. Rev. B*, **19**, 5754–5772.

FEJES, P. L. (1977). *Acta Cryst.* A**33**, 109–113.

FUJIWARA, K. (1957). *J. Phys. Soc. Jpn*, **12**, 7–13.

GOODMAN, P. & MOODIE, A. F. (1974). *Acta Cryst.* A**30**, 280–290.

HOSHINO, S. & MOTEGI, H. (1967). *Jpn. J. Appl. Phys.* **6**, 708–718.

IIJIMA, S. & COWLEY, J. M. (1974). *J. Phys. C*, **7**, 135–144.

IIZUMI, M., AXE, J. D., SHIRANE, G. & SHIMAOKA, K. (1977). *Phys. Rev. B*, **15**, 4392–4411.

ISHIZAWA, N., MARUMO, F. & IAWAI, S. (1980). *Acta Cryst.* B**36**, 763–766.

ISHIZAWA, N., MARUMO, F., KAWAMURA, T. & KIMURA, M. (1975). *Acta Cryst.* B**31**, 1912–1915.

ISHIZUKA, K. (1982). *Acta Cryst.* A**38**, 773–779

NAKAZAWA, H., YAMAMOTO, A. & MORIMOTO, M. (1979). *AIP Conf. Proc.* No. 53, pp. 358–360.

NANAMATSU, S., KIMURA, M., DOI, K. & TAKAHASHI, M. (1971). *J. Phys. Soc. Jpn*, **30**, 300–301.

NANAMATSU, S., KIMURA, M. & KAWAMURA, T. (1975). *J. Phys. Soc. Jpn*, **38**, 817–824.

OHI, K., KIMURA, M., ISHIDA, H. & KAKINUMA, H. (1979). *J. Phys. Soc. Jpn*, **46**, 1387–1388.

SATO, H. & TOTH, R. S. (1961). *Phys. Rev.* **124**, 1833–1847.

SCHEUNEMANN, K. & MÜLLER-BUSHBAUM, H. (1975). *J. Inorg. Nucl. Chem.* **37**, 1679–1680.

SHIOZAKI, Y. (1971). *Ferroelectrics*, **2**, 245–260.

TAKAHASHI, M., NANAMATSU, S. & KIMURA, M. (1972). *J. Cryst. Growth*, **13/14**, 681–685.

VAN LANDUYT, J., VAN TENDELOO, G. & AMELINCKX, S. (1974*a*). *Phys. Status Solidi A*, **26**, 359–376.

VAN LANDUYT, J., VAN TENDELOO, G. & AMELINCKX, S. (1974*b*). *Phys. Status Solidi A*, **26**, 585–592.

VAN LANDUYT, J., VAN TENDELOO, G. & AMELINCKX, S. (1976). *Phys. Status Solidi A*, **36**, 757–777.

WILSON, J. A., DI SALVO, F. J. & MAHAJAN, S. (1975). *Adv. Phys.* **24**, 117–201.

YAMAMOTO, N., NAKAMURA, M., YAGI, K. & OHI, K. (1980). *J. Phys. Soc. Jpn*, **49**, Suppl. B, 95–97.

YAMAMOTO, N., YAGI, K., HONJO, G., KIMURA, M. & KAWAMURA, T. (1980). *J. Phys. Soc. Jpn*, **48**, 185–191.